

REAL STRUCTURE  
OF CRYSTALS

# Modification of the Crystal Structure of Gadolinium Gallium Garnet by Helium Ion Irradiation

B. K. Ostafiychuk<sup>a</sup>, I. P. Yaremiy<sup>a</sup>, S. I. Yaremiy<sup>a</sup>, V. D. Fedoriv<sup>a</sup>, U. O. Tomyn<sup>a</sup>, M. M. Umantsiv<sup>a</sup>, I. M. Fodchuk<sup>b</sup>, and V. P. Kladko<sup>c</sup>

<sup>a</sup> Vasyl Stefanyk Precarpathian National University, Shevchenko st. 57, Ivano-Frankivsk 76018, Ukraine  
e-mail: yaremiy@rambler.ru

<sup>b</sup> Fedkovych State University, Kotsyubinskogo st. 2, Chernivtsi 58012, Ukraine

<sup>c</sup> Lashkaryov Institute of Semiconductor Physics, National Academy of Sciences of Ukraine, Nauki pr. 41, Kiev, 03028, Ukraine

Received February 22, 2012

**Abstract**—The structure of gadolinium gallium garnet (GGG) single crystals before and after implantation by He<sup>+</sup> ions has been investigated using high-resolution X-ray diffraction methods and the generalized dynamic theory of X-ray scattering. The main types of growth defects in GGG single crystals and radiation-induced defects in the ion-implanted layer have been determined. It is established that the concentration of dislocation loops in the GGG surface layer modified by ion implantation increases and their radius decreases with an increase in the implantation dose.

DOI: 10.1134/S1063774513070122

## INTRODUCTION

Gadolinium gallium garnet (GGG, Gd<sub>3</sub>Ga<sub>5</sub>O<sub>12</sub>) single crystals are widely used as substrates for garnet ferrite films which are applied in microwave electronics, magneto-optics, magnetic field sensors, optoelectronics (phosphors for LEDs), and solid-state lasers in the IR and visible ranges. In addition, they are convenient model samples with a complex basis for studying the physics of the processes occurring in their bulk and in the surface layer.

Ion implantation is one of the most promising methods for affecting surface layers of single crystals in order to deliberately impart particular properties to them. In particular, implantation by He<sup>+</sup> ions makes it possible to significantly increase the thickness of modified layer without its significant amorphization. A surface waveguide layer is formed in GGG single crystals by ion implantation.

Structural inhomogeneities caused by both growth and radiation-induced defects in GGG single crystals, as well as the kinetics of their interaction, have a determining influence on the operating characteristics of elements of GGG-based devices. Therefore, studying the defect subsystem in initial and modified GGG single crystals is an urgent problem.

## EXPERIMENTAL

The objects of study were GGG single-crystal plates 0.49 mm thick grown by the Czochralski method in the (111) direction. The postgrowth treatment of the plates included mechanical grinding and mechanical, mechanochemical, and chemical polish-

ing; after the final treatment the surface had the 14th grade of finish.

GGG single crystals were implanted by 100-keV He<sup>+</sup> ions under conditions excluding channeling (at an angle of ~7° with respect to the normal to the surface). To minimize the self-annealing effect, the density of the ion current did not exceed 0.2 μA/cm<sup>2</sup> during implantation.

The defect structure of real GGG crystals with microdefects of different sizes and concentrations can be investigated in a rapid and nondestructive way using X-ray diffraction methods [1–3].

Rocking curves and equal-intensity contours for GGG single crystals were recorded on a high-resolution X'Pert PRO MRD XL X-ray diffractometer in CuK<sub>α1</sub> radiation. Rocking curves from the (444) and (888) planes were obtained in the ω/2θ-scan mode using the triple-crystal scheme and the [omega]-scan mode in double- and triple-crystal geometries [4].

## GROWTH DEFECTS IN GGG SINGLE CRYSTALS

Figure 1 shows double-crystal rocking curves recorded in the ω-scan mode and triple-crystal rocking curves recorded in the ω/2θ- and ω-scan modes with an immobile analyzer. One can see that all rocking curves are symmetric. The curve broadening in the ω-scan mode is insignificant in comparison with the ω/2θ-scan curves; this fact indicates that GGG plates are single crystals.

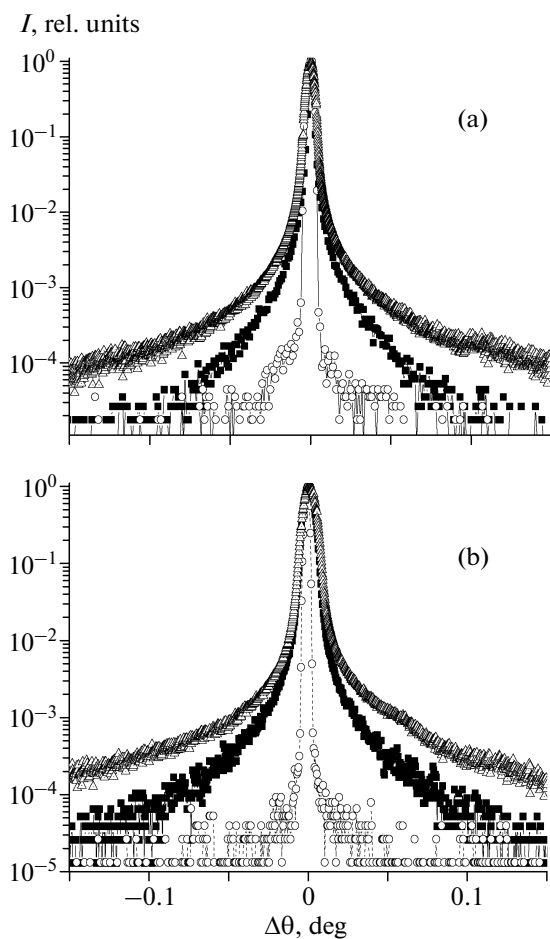


**Fig. 1.** Rocking curves from the (a) (444) and (b) (888) planes recorded in the (■)  $\omega/2\theta$ -scan mode, triple-crystal geometry; (○)  $\omega$ -scan mode, triple-crystal geometry; and (△)  $\omega$ -scan mode, double-crystal geometry.

Two-dimensional intensity maps in the  $\omega$  and  $2\theta$  coordinates show the absence of any significant diffuse scattering component (Fig. 2).

An analysis of the half-widths of rocking curves along and across the diffraction vector direction showed that physical broadening X-ray lines, which is typical of II-class defects (in Krivoglaz's classification), is practically absent; therefore, the influence of defects of this type on the rocking curves can be neglected. Therefore, in further analysis we took into account the data on the diffuse scattering caused by only defects of class I.

Thus, the simulation of X-ray propagation in materials under study must be performed with regard to the lattice defects existing in them.

Generally, X-ray scattering occurs from defects (diffuse component) and the "quasi-ideal" part of single crystal (coherent component). Depending on the collection method, one or both components of scattered X rays are taken into consideration.

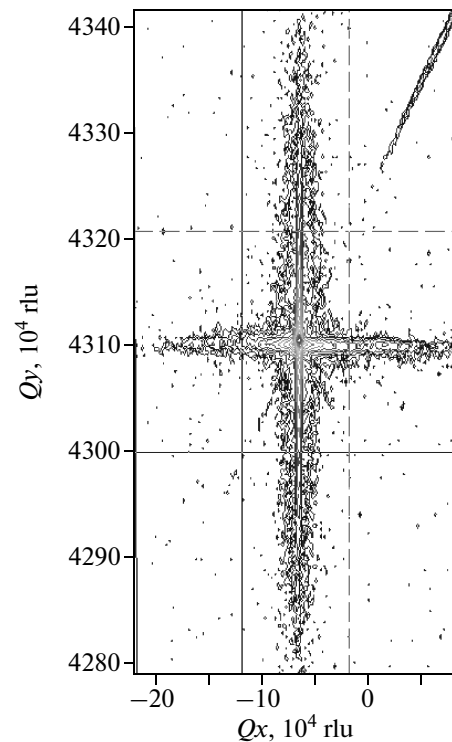


**Fig. 2.** Reciprocal space map for a GGG single crystal near the (444) site.

When simulating the rocking curves recorded on a double-crystal spectrometer with a widely open detector window, rocking curves were calculated as the sum of coherent ( $R_{coh}$ ) and diffuse ( $R_{diff}$ ) components:

$$R(\Delta\theta) = R_{coh}(\Delta\theta) + R_{diff}(\Delta\theta).$$

The increase in the diffuse-scattering intensity with an increase of the concentration and size of defects correspondingly changes the coherent-component intensity. The coherent and diffuse components were calculated within the generalized dynamic theory of X-ray scattering according to [5, 6].

It was assumed that a specimen under study may contain growth defects of different types. However, the attempts to improve agreement between the experimental and theoretical rocking curves under the assumption of the existence of spherical or disk-shaped clusters were not successful because of the radically different behavior of the rocking-curve tails for defects of these types.

The best agreement between the theoretical and experimental rocking curves is obtained when dislocation loops of certain sizes are taken into consideration. However, the introduction of only small loops into the model led to good consistency only on the rocking-curve tails (far from the main Bragg peak). The introduction of only large loops provided good agreement in the vicinity of the main Bragg peak but rather high inconsistency on the tails. The optimum was observed

Concentrations and sizes of dislocation loops

HKL	Size, Å	Concentration, cm <sup>-3</sup>	Size, Å	Concentration, cm <sup>-3</sup>
444	50	1 × 10 <sup>15</sup>	6000	1.2 × 10 <sup>10</sup>
888	54	1 × 10 <sup>15</sup>	5900	1.1 × 10 <sup>10</sup>

when dislocation loops of two sizes were introduced; their parameters are listed in the table for the (444) and (888) reflections.

Figure 3 presents an example of the total theoretical rocking curve with allowance for instrumental broadening and an experimental rocking curve for the sizes and defect concentrations listed in the table.

A simulation of ω/2θ rocking curves for defects of certain types and their comparison with the corresponding experimental rocking curves showed their good coincidence both near the main Bragg peaks and on the tails.

The adequacy of the chosen model of the defect subsystem is confirmed by agreement between the theoretical and experimental rocking curves obtained in different scan modes and different reflections.

### RADIATION-INDUCED DEFECTS IN GGG SINGLE CRYSTALS IMPLANTED BY HE<sup>+</sup> IONS

The lattice deformation in GGG single crystals affects, for example, the refractive index of the waveguide layer; therefore, its analysis is important to

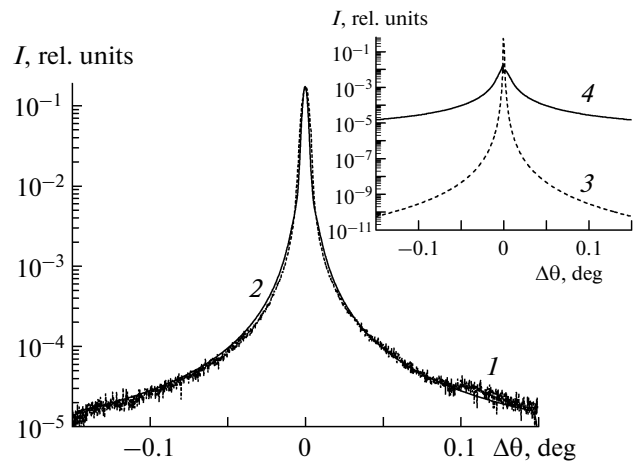


Fig. 3. (1) Experimental and (2) theoretical (with allowance for instrumental broadening) rocking curves for a GGG single crystal in the (444) reflection. The inset shows the (3) coherent and (4) diffuse components of the theoretical rocking curve.

ensure undisturbed device operation. This analysis meets a number of problems. In particular, the depth distribution of the strain can be obtained from rocking curves for symmetric reflections (444) and (888). However, the change in the interplanar spacing in the plate plane (which determines the strained state of layered structure) is rather difficult to determine even from asymmetric reflections (for example, (880)) because of insufficient accuracy. Therefore, reciprocal space maps were plotted to obtain the necessary data (Fig. 4) [7].

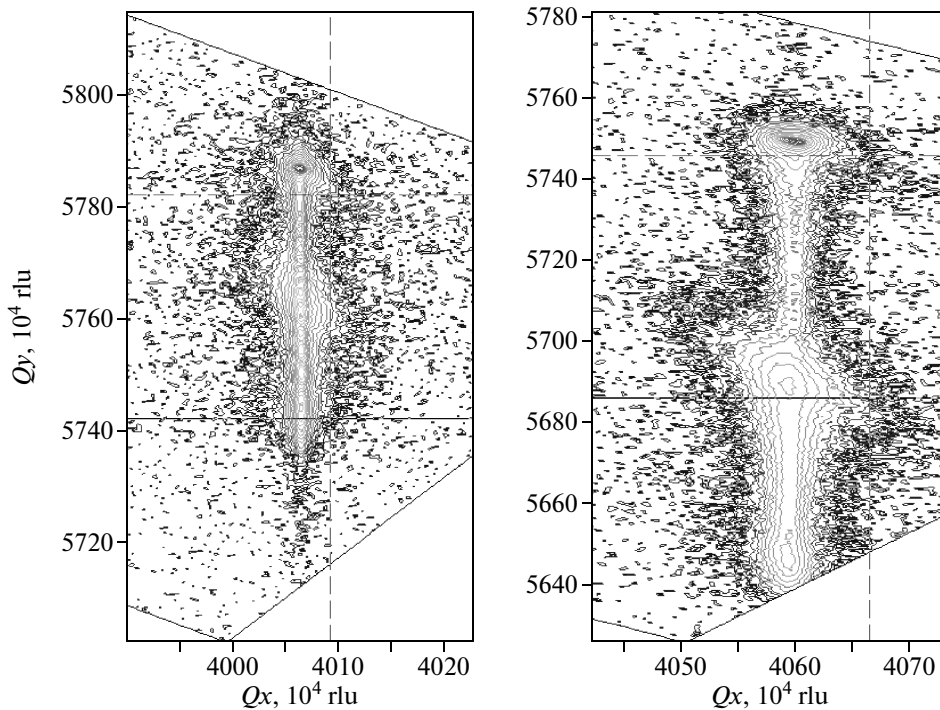


Fig. 4. Reciprocal space maps for He<sup>+</sup>-ion implanted GGG single crystals near the (880) site; implantation dose  $D =$  (a)  $2 \times 10^{15}$  and (b)  $6 \times 10^{15}$  cm<sup>-2</sup>.

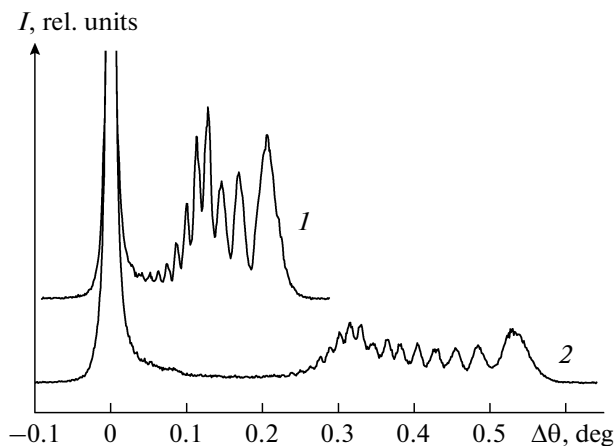


Fig. 5. Experimental rocking curves for GGG single crystals implanted by 100-keV  $\text{He}^+$  ions to doses of (1)  $2 \times 10^{15}$  and (2)  $6 \times 10^{15} \text{ cm}^{-2}$ .

The reciprocal space maps of GGG single crystals implanted by  $\text{He}^+$  ions (Fig. 4) show that the intensity distribution in the plate plane corresponds to the theoretical width. Although the interplanar spacing changes along the implanted-layer depth (i.e., in the direction perpendicular to the plate plane), it barely changes over the plane of implanted layer (Fig. 4). Thus, we can conclude that the ion-implanted layers in GGG single crystals are in the completely strained state in the plate plane.

The rocking curves for GGG single crystals implanted by  $\text{He}^+$  ions contain, along with the intense peak from the region undisturbed by implantation, weak oscillations from X rays scattered by the deformed surface layer (Fig. 5); this pattern is in agreement with the reciprocal space maps.

The theoretical rocking curves for ion-implanted GGG single crystals were calculated on the assumption of the presence of point defects and dislocation loops in the damaged layer. The point defects in the substrate and damaged layer were modeled by spherical clusters 10 Å in size. With allowance for nonuniform defect distribution (typical of ion-implanted layers), the surface layer was divided into sublayers, each characterized by constant strain and uniform defect distribution. The atomic displacements in each sublayer caused by radiation-induced defects in other sublayers were disregarded. The amplitude of the coherent component from the ideal part of single crystal was calculated within the generalized dynamic theory [5, 6] and the component from the damaged layer was found using the Takagi equations for a discrete-layered structure [8].

In the case of scattering by a thin crystal, the diffuse component from the damaged layer can be presented as a sum of diffuse components of the reflection coefficients of substrate ( $R_{diff}^S$ ) and damaged layer ( $R_{diff}^L$ ):

$$R_{diff}(\Delta\theta) = R_{diff}^S(\Delta\theta) + R_{diff}^L(\Delta\theta).$$

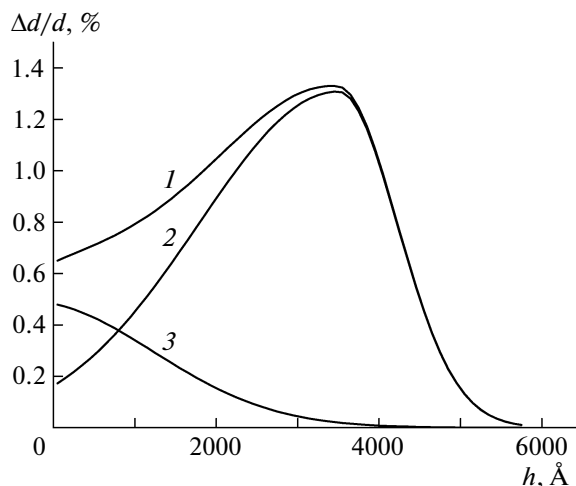


Fig. 6. (1) Strain profile in the surface layer of  $\text{He}^+$ -ion implanted GGG single crystals and its components due to (2) nuclear and (3) electron energy loss of implanted ion ( $E = 100 \text{ keV}$ ,  $D = 4 \times 10^{15} \text{ cm}^{-2}$ ).

When calculating  $R_{diff}^S$ , the X-ray absorption in the damaged layer was taken into consideration according to [9].

The strain profiles were calculated under the assumption of their proportionality to the profile of radiation-induced defects (this holds true for low implantation doses). The latter, in turn, can be presented as a sum of two components. The first is due to the nuclear energy loss (described by an asymmetric Gaussian) and the second is related to the electron energy loss (described by a decreasing Gaussian). Therefore, the strain profile in GGG surface layers implanted by light ions was specified as the sum of asymmetric and decreasing Gaussians:

$$\frac{\Delta d}{d}(h) = \begin{cases} \left. \frac{\Delta d}{d} \right|_{n\max} \exp \left[ -\left( \frac{h - R_{pn}}{w_{n1}} \right)^2 \right] & \text{at } h < R_{pn} \\ \left. \frac{\Delta d}{d} \right|_{n\max} \exp \left[ -\left( \frac{h - R_{pn}}{w_{n2}} \right)^2 \right] & \text{at } h \geq R_{pn} \end{cases}$$

$$\left. \frac{\Delta d}{d} \right|_{e\max} \exp \left[ -\left( \frac{h - R_{pe}}{w_e} \right)^2 \right],$$

where  $h$  is the distance counted from the crystal surface into the bulk;  $R_{pn}$  is the junction of the Gaussian branches; and  $w_{n1}$ ,  $w_{n2}$ , and  $w_e$  are the parameters of Gaussians, which characterize their FWHM. The subscripts  $n$  and  $e$  refer to the strain profile components that are related, respectively, to the nuclear and electron energy losses of implanted ion.

Using the abovementioned function and deliberately changing its parameters with the aid of a specially developed program, we calculated the strain profiles, which turned out to be of the same type in the entire dose range under study (Fig. 6). The maximum strain

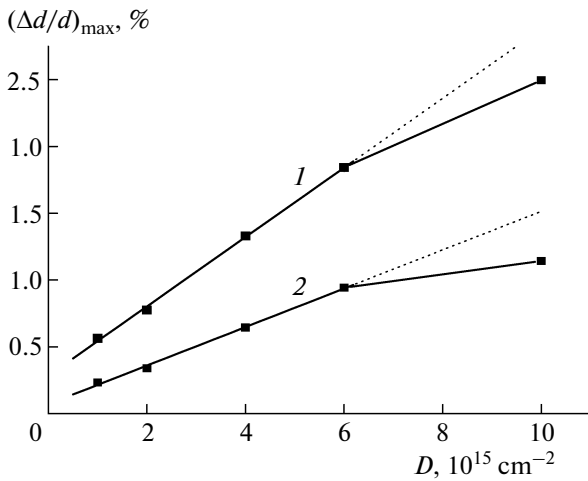


**Fig. 7.** Dose dependences of the (1) maximum strain and (2) the strain on the surface for GGG single crystals implanted by  $\text{He}^+$  ions ( $E = 100 \text{ keV}$ ).

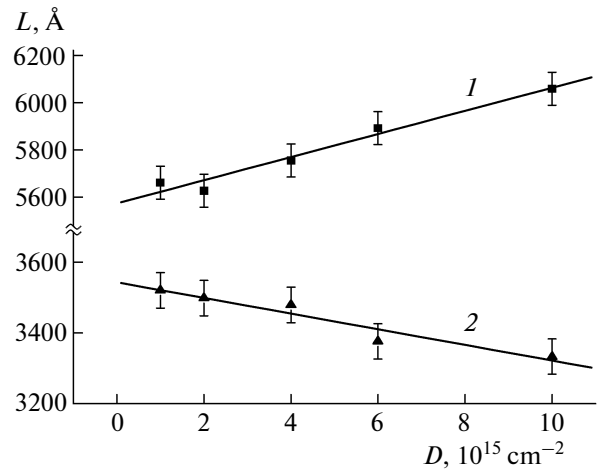


**Fig. 8.** Dose dependences of (1) the deformed layer thickness  $L$  and (2) the position of maximum strain  $R_p$  for GGG single crystals implanted by  $\text{He}^+$  ions.

and the strain on the surface change linearly in the dose range from  $1 \times 10^{15}$ – $6 \times 10^{15} \text{ cm}^{-2}$  (Fig. 7); at higher doses the linearity is violated, which indicates the onset of overlap of displaced-atom cascades. The thickness of the deformed layer in GGG single crystals insignificantly increases with an increase in the implantation dose (Fig. 8) and the position of the strain peak shifts to the surface. The extreme value of the static factor  $E = e^w$  (the value in the region of maximum strain) linearly decreases with an increase in the implantation dose, although this linearity is violated for implantation doses above  $6 \times 10^{15} \text{ cm}^{-2}$ .

The theoretical rocking curves of implanted samples were simulated with the generalized dynamic theory of X-ray scattering taking into account the presence of defects (see table) in the unimplanted part of single crystals.

Complex defects in the ion-implanted layer were modeled by dislocation loops, the radius and concentration of which were assumed to be described by the corresponding strain profiles. The parameters of the dislocation loops in the maximally strained layer, estimated from experimental rocking curves (444), are characterized by several sets of radius  $R$  and concentration  $n$ , which yield satisfactory agreement between the theoretical and experimental rocking curves. The dependences  $n(R)$  for dislocation loops on a logarithmic scale are linear for different implantation doses (Fig. 9).

Experimental rocking curves (888) were recorded in the  $\omega$ - and  $\omega/2\theta$ -scan modes to refine the information about the parameters of the defect structure of the ion-implanted layer. The static factor  $E$  for the (888) reflections is less than that for the (444) reflections by  $\sim 20\%$ . This difference manifests itself in the decrease in the coherent component intensity and a rise in the diffuse component intensity; it can be used to reduce

the error in determining the defect subsystem parameters. In the rocking curves this is especially pronounced in the last oscillation, which corresponds to the maximum strain.

The experimental and theoretical rocking curves are in the best agreement at the dislocation loop parameters presented in Fig. 10. The radius of dislocation loops decreases and their concentration increases with an increase in the implantation dose, which is why the static Debye–Waller factor  $L$  and the diffuse scattering intensity rise.

An example of a rocking curve which corresponds to the defect parameters at the best correspondence between the theoretical and experimental rocking curves for the (444) reflection is shown in Fig. 11. One

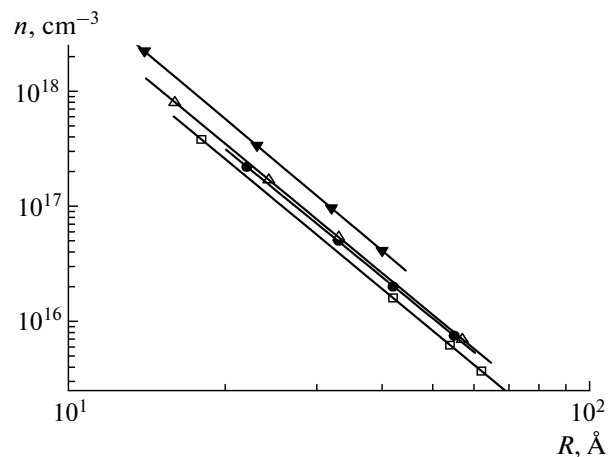


**Fig. 9.** Dependences of the concentration of dislocation loops in the maximally strained layer of GGG single crystal on their radius at different  $\text{H}^+$ -ion implantation doses: ( $\square$ )  $2 \times 10^{15}$ , ( $\bullet$ )  $4 \times 10^{15}$ , ( $\triangle$ )  $6 \times 10^{15}$ , and ( $\blacktriangledown$ )  $1 \times 10^{16} \text{ cm}^{-2}$ .

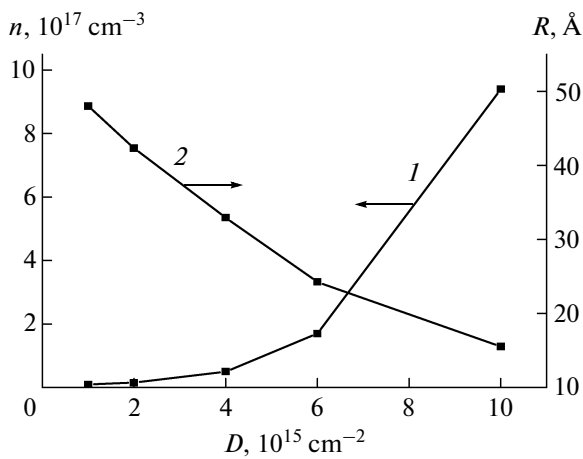


**Fig. 10.** Dependences of the (1) concentration and (2) radius of dislocation loops in the maximally strained layer of  $\text{He}^+$ -ion implanted GGG single crystals on the implantation dose.

can see that the shape of the background after the last oscillation on the rocking curve tail is decisive in the calculations.

The dependences can be explained based on the results of SRIM-2008 simulation of the  $\text{He}^+$ -ion implantation of GGG single crystals. This simulation revealed that each transit of implanted ion leads to the formation of three to five regions, each containing more than ten knocked-out matrix ions. Obviously, these disordered regions become centers of dislocation loop nucleation. As the irradiation dose is accumulated, the number of these centers increases and the size of the dislocation loops formed from them decreases due to the increase in the number of possible sinks for single defects.

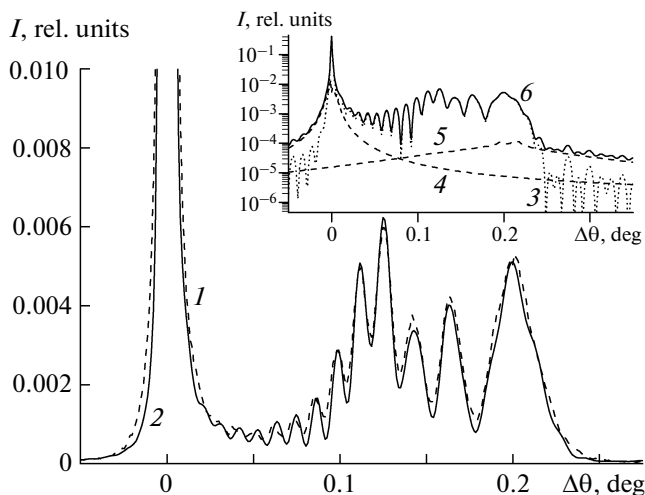


**Fig. 11.** (1) Experimental and (2) theoretical (with allowance for instrumental broadening) (444) rocking curves for a GGG single crystal implanted by  $\text{He}^+$  ions to a dose of  $2 \times 10^{15} \text{ cm}^{-2}$ . The inset shows the (3) coherent, (4) diffuse (from the substrate), and (5) damaged layer components of the theoretical rocking curve and (6) their sum.

## CONCLUSIONS

The complex study of GGG single crystals by double- and triple-crystal X-ray diffractometry showed that they contain mainly I-class defects (according to Krivoglaz's classification). The main type of growth defects is dislocation loops with average sizes of 60 and 6000 Å.

The strain profiles in GGG single crystals implanted by  $\text{He}^+$  ions ( $E = 100 \text{ keV}$ ) to doses of  $1 \times 10^{15} - 1 \times 10^{16} \text{ cm}^{-2}$  are of the same type: the damaged layer thickness insignificantly increases with an increase in the implantation dose and the position of the maximum strain shifts to the surface. The maximum strain and the strain on the surface change linearly in the dose range of  $1 \times 10^{15} - 6 \times 10^{15} \text{ cm}^{-2}$ . This linearity is violated with a further increase in dose, which indicates the onset of an interaction between radiation-induced defects.

The main types of radiation-induced defects generated in the surface layers of GGG single crystals during  $\text{He}^+$ -ion implantation are point defects and dislocation loops with average sizes of 30–70 Å. With the increase in the implantation dose, the concentration of dislocation loops increases and their radius decreases.

Despite the large values of relative strain in the direction perpendicular to the plate plane (up to 3%), the state in the plates plane of GGG single crystals implanted by  $\text{He}^+$  ions is completely strained and the lattice symmetry in the ion-implanted layer transformed from cubic to rhombohedral (the angle with a rhombohedron vertex  $\alpha < 90^\circ$ ).

## REFERENCES

1. M. A. Krivoglaz, *Diffraction of X-rays and Neutrons in Non-ideal Crystals* (Naukova Dumka, Kiev, 1983) [in Russian].
2. V. B. Molodkin, A. I. Nizkova, A. P. Shpak, et al., *Diffractometry of Nanoscale Defects and Heterolayers in Crystals* (Akademperiodika, Kiev, 2005) [in Russian].
3. A. L. Golovin, R. M. Imamov, and E. A. Kondrashkina, *Phys. Status Solidi A* **88**, 505 (1985).
4. V. B. Molodkin, V. P. Klad'ko, S. I. Olikhovskii, et al., *Metallofiz. Noveishie Tekhnol.* **31** (9), 1205 (2009).
5. V. B. Molodkin, S. I. Olikhovskii, E. N. Kislovskii, et al., *Phys. Status Solidi B* **227** (2), 429 (2001).
6. S. I. Olikhovskii, V. B. Molodkin, E. N. Kislovskii, et al., *Phys. Status Solidi B* **231** (1), 199 (2002).
7. O. M. Efanov, V. P. Klad'ko, V. F. Machulin, et al., *Dynamic X-Ray Diffraction in Multilayer Structures* (Naukova dumka, Kiev, 2008) [in Russian].
8. M. V. Kovalchuk, V. G. Kohn, and E. F. Lobanovich, *Fiz. Tverd. Tela* **27** (11), 3379 (1985).
9. S. I. Olikhovskii, V. B. Molodkin, E. N. Kislovskii, et al., *Metallofiz. Noveishie Tekhnol.* **27** (5), 653 (2005).
10. B. Ostafiichuk, V. D. Fedorov, S. I. Yaremii, et al., *Metallofiz. Noveishie Tekhnol.* **30** (9), 121 (2008).

Translated by Yu. Sin'kov